Journal of Alloys and Compounds 690 (2017) 360–368

Contents lists available at ScienceDirect

Journal of Alloys and Compounds

journal homepage: http://www.elsevier.com/locate/jalcom

Thermal processing of aqueous AZO inks towards functional TCO thin films

Kenny Vernieuwe [a], Dieter Cuypers [b], Christine E.A. Kirschhock [c], Kristof Houthoofd [c], Henk Vrielinck [d], Johan Lauwaert [e], Jonathan De Roo [a], José C. Martins [f], Isabel Van Driessche [a], Klaartje De Buysser [a, *]

[a] SCRiPTS, Department of Inorganic and Physical Chemistry, Ghent University, Krijgslaan 281-S3, 9000 Ghent, Belgium
[b] Centre for Microsystems Technology (CMST), IMEC and Ghent University, Technologiepark 914, 9052, Ghent, Belgium
[c] Center for Surface Chemistry and Catalysis, KU Leuven, Leuven, Belgium
[d] DiSC, Department of Solid State Sciences, Ghent University, Krijgslaan 281-S1, 9000, Ghent, Belgium
[e] Department of Electronics and Information Systems (ELIS), Ghent University, St.-Pietersnieuwstraat 41, B-9000, Ghent, Belgium
[f] NMR and Structural Analysis Unit, Department of Organic and Macromolecular Chemistry, Ghent University, Krijgslaan 281-S4, 9000, Ghent, Belgium

ARTICLE INFO

Article history:
Received 10 May 2016
Received in revised form
26 July 2016
Accepted 15 August 2016
Available online 18 August 2016

Keywords:
Al-doped ZnO
Thin film
Inkjet printing
Transparent conductors
Sol-gel

ABSTRACT

Aluminium doped zinc oxide is considered an interesting, earth abundant alternative to the transparent conductor indium tin oxide. In this respect, we synthesized Al-ZnO (AZO) thin films by a chemical solution deposition approach. Using water-based inks, the AZO thin films were printed in one single step on glass substrates in non-vacuum conditions. The drying process and the humidity of the atmosphere proved to be crucial during the thermal processing of the wet deposited thin films. To improve the understanding of the phenomena involved, the influence of these processing parameters on the final properties of the AZO thin films are investigated by FTIR, XRD, SEM, ^{1}H and ^{27}Al NMR and resistivity measurements. Optimal conditions were obtained by drying the wet thin film at 120 °C, followed by heating in a tube furnace until 500 °C under a 200 ppm O_2/N_2 atmosphere with a humidity controlled by bubbling the gas flow through 2 glass bottles containing water at 20 °C. AZO thin films with an resistivity of 2.54×10^{-2} Ω cm were obtained.

1. Introduction

Indium tin oxide (ITO) is generally accepted as the leading transparent conductive oxide (TCO) [1]. However, an expanding market of TCOs and an unstable supply of indium stirred research efforts towards indium free TCOs. Indeed, indium's natural scarcity and the increasing demand for ITO resulted in a soaring market value for indium. Before 1960 the price of indium metal was steady at $72/kg but rose to $735/kg in 2014. N-type doped ZnO is an attractive candidate for indium free TCO with Al and Ga as promising dopants [2–4]. Doping ZnO with group IIIA elements such as B, Al, Ga, In lowers the resistivity and increases the carrier density. Al, Ga, and In are the most frequently used dopants. We favour Al as dopant for the ZnO host matric for several reasons. (1) The introduction of Al in the host matric under reducing conditions creates defect levels close to the ZnO conduction band [5]. (2) The experimental solubility limit of 3–4 at% allows the introduction of a large quantity of charge carriers [6–8]. (3) Al is the most cheap and abundant element of group IIIA [9].

A dopant can occupy diverse sites in the crystal structure of the host matrix; (i) empty octahedral or (ii) empty tetrahedral sites. Alternatively, (iii) a dopant ion can substitute Zn in the regular lattice. In the latter case, the dopant occupies a tetrahedral site and can donate a free electron to the conduction band of ZnO [10]. In contrast, if an *interstitial* tetrahedral site is occupied, the dopant is inactive, whereas occupied octahedral sites act as electron acceptors [10,11]. These doped ZnO materials have the capacity to reach competitive opto-electrical properties compared to ITO [12,13]. Nevertheless, the manufacturing process of doped ZnO thin films still lacks high throughput capacity. In addition, commonly used vacuum deposition methods such as chemical vapor deposition (CVD), sputtering, pulsed laser deposition (PLD) suffer from by high cost associated with maintaining vacuum during production [14].

* Corresponding author.
E-mail address: Klaartje.debuysser@ugent.be (K. De Buysser).

http://dx.doi.org/10.1016/j.jallcom.2016.08.120
0925-8388/

Although the nowadays studied chemical solution deposition (CSD) processes are better, they often apply multiple coatings steps with an intensive thermal treatment in between [15–18].

In this paper, we opted to investigate the synthesis of Al doped ZnO (AZO) thin films due the high abundance and low cost of Al and Zn and its excellent opto-electrical properties [9]. Our goal is to deposit AZO thin films through CSD processing in an environmental friendly and scalable manner. As deposition method, ink jet printing is selected and the AZO thin films are synthesized through the single deposition of an aqueous ink. Ink jet printing is a scalable and versatile technique which allows a controlled deposition of thin films and patterns on small or large surfaces [19,20]. Ink jet printers have a closed cartridge which reduces any chance of contamination and the precise deposition of the droplets reduce undesired waste of the ink. The synthesis of aqueous inks avoids the commonly used toxic organic solvents such as 2-methoxyethanol. However, dissolving metal precursors in water enhances the possibility of metal hydroxide precipitation at neutral pH levels [21–23]. Stable inks are obtained by adding chelating components such as ethylenediaminetetraacetic acid (EDTA), citric acid (CA), nitrilotriacetic acid (NTA), etc. These additives make the thermal processing of wet thin films more complex. The development and characterisation of the inks and the printing itself was studied in detail in a previous paper [24]. Optimising the processing steps such as drying time, synthesis temperature, humidity of the used atmosphere aims to further improve the final morphology and properties of the films and is the subject of this paper.

2. Experimental section

2.1. Synthesis

The preparation of the AZO ink, cleaning of the substrates and deposition of the ink are discussed in detail elsewhere [24]. Two separate aqueous solutions were prepared containing stabilized Zn^{2+} and Al^{3+} ions. The Zn solution contains zinc acetate (0.5 mol L^{-1}), ethanolamine, formic acid, while the Al solution contains aluminium nitrate (0.5 mol L^{-1}), malonic acid, ethanolamine and formic acid. Mixing both solutions resulted in a stable AZO aqueous ink which could be printed by the addition of 10 v% of ethanol.

The AZO thin films were printed on cleaned EAGLE^{2000} glass substrates (Präzisions Glass&Optics) with a piezoelectric drop-on-demand printing system and a computer controlled XY plotter. The orifice used (Microfab, MJ-ABP-01) had a diameter of 30 μm. The ink was jetted at 2 kHz. The applied waveform had a maximum of 14 V that was maintained for 4 μs A thin film was printed with a line and drop spacing of 50 μm.

The printed layers were dried on a preheated hotplate for 10 min at varying temperatures (90–250 °C) before thermal treatment in a tube furnace till 500 °C in a wet or dry 200 ppm O_2/N_2 atmosphere. The heating rate was kept at 10 °C/min with a dwell at 250 °C and 500 °C for 1 h. The wet atmosphere was established by bubbling the dry atmosphere through 2 glass bottles containing water at varying temperatures. By controlling the water temperature, the amount of water vapour carried with the atmosphere was altered. Finally, samples were postheated at 450 °C during 30 min in a dry Ar/5% H_2 atmosphere to create more charge carries in order to enhance the electrical properties [25,26].

2.2. Characterization

The precursor solutions were studied by NMR (Bruker Avance III Spectrometer operating at a ^{1}H frequency of 500.13 MHz and equipped with a BBI_Z gradient probe) and ATR-FTIR (Perkin Elmer Spectrum 100). Except mentioned otherwise, the FTIR measurements were performed on dried inks and metal-ion free blanks at 75 °C. The 1D ^{1}H NMR spectra recorded after heating the ink and required dilution in D_2O till the initial concentration of the precursor was obtained. Diffusion NMR measurements (2D DOSY) were performed on as prepared metal-ion free blanks and inks using a double stimulated echo sequence for convection compensation and with monopolar gradient pulses. Smoothed rectangle gradient pulse shapes were used throughout. The gradient strength was varied quadratically from 2 to 95% of the probe's maximum value (calibrated at 50.2 G/cm) in 32 or 64 steps, with the gradient pulse duration and diffusion delay optimized to ensure a final attenuation of the signal in the final increment of less than 10% relative to the first increment.

1D^{27}Al MAS NMR was used to study the influence of dry and wet thermal processing on the Al incorporation in the ZnO matrix. AZO bulk powders were synthesised in dry or wet air at 500 °C. The wet processed AZO powders were synthesised by bubbling the used gas flow through 2 glass bottles at 20 °C during synthesis. The spectra were recorded on a Bruker Avance400 spectrometer, using a 4 mm MAS probe and a spinning frequency of 10 kHz. The length and power level of the rf-pulses were carefully optimised on the sample itself. The collected data are an accumulation of 1536 scans with a recycle delay of 5s.

TGA/DTA measurements were performed on a Netzsch STA449 F3 Jupiter setup. The samples were dried at 75 °C during 1 h prior to analysis. A quantity of ±10 mg of material was heated at 10 °C/min under a 120 mL/min air flow.

The morphology of the processed AZO coatings was analysed with a FEI Nova 600 Nanolab Dual Beam FIB-SEM. The crystalline phases of the obtained AZO coatings were characterised using a powder X-ray diffractometer equipped with a line detector and Cu K_α ($\lambda = 0.154$ nm) radiation (Bruker D8 Discover). The sheet resistance was measured by a four point wafer prober (Veeco, FPP-5000) while the carrier concentration and mobility were measured with a home-built setup in the Hall-Van der Pauw configuration (Keithley 6220 Precision Current Source, HP 3478 A Multimeter, electromagnet Varian V 3603).

3. Results and discussion

Previous results showed that the synthesized AZO thin films have a minimum resistivity when doped with 3 at% of Al. The final processed AZO layer using the printing parameters mentioned in the experimental section had a thickness of 80 nm. The doping percentages nor the printing parameters were varied in this paper.

3.1. Influence of the drying temperature on the formation of AZO thin films

After ink-jet printing of the precursor solution, the samples were first dried on a hotplate before the final thermal treatment in a tube furnace. This drying step was performed at various temperatures and related to the resistivity of the final layer (Fig. 1). From the figure, it is clear that the optimal drying temperature was 120 °C as this coincides with a minimum in resistivity.

To elucidate the chemical reactions that occur during the drying step, we studied the AZO films with a combination of FTIR and NMR. The inks were studied first to identify the formed complexes. The FTIR spectra of the ink dried at 75 °C (Fig. 2A) did not show a clear presence of the possibly formed Zn complexes and signals of Al complexes are absent due to the low concentration of these species in the ink. A small shift in the ν_a (COO) and ν_s (COO) of the formate and the acetate group suggest the formation of Zn acetate and formate complexes (Table 1). Therefore, the Al and Zn

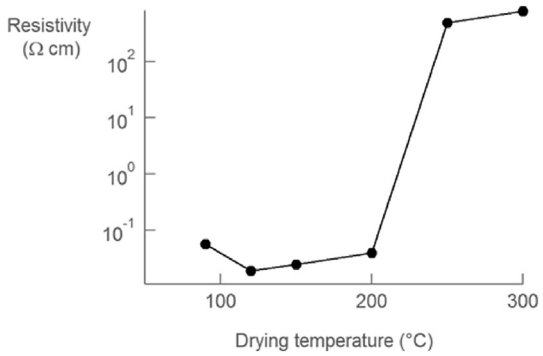

Fig. 1. Resistivity of AZO thin films prepared at different drying temperature before the oxidative thermal treatment took place. (identical for all samples: 450 °C during 30 min in a Ar/5% H_2 atmosphere).

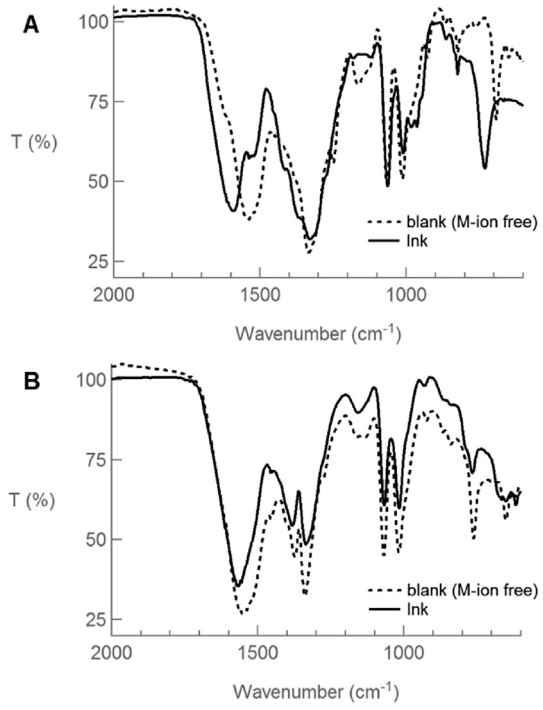

Fig. 2. A) FTIR measurement of the ink (solid line) and metal-ion free blank (dashed line). B) FTIR measurement of the Al precursor solution (solid line) and blank (metal-ion free) (dashed line).

precursor solutions were studied separately. Compared to the blank (metal-ion free), the FTIR spectrum of the Al precursor solution (Fig. 2B) shows a clear shift of the ν_a (COO) and ν_s (COO) of malonic acid, respectively from 1538 to 1592 cm^{-1} and 1334 to 1308 cm^{-1}. In the fingerprint of the spectra an obvious shift of the ρ_r (COO) of malonic acid is visible, respectively from 692 to 732 cm^{-1} (Table 2). This all confirms the chelating behaviour of malonic acid and the formation of Al malonate complexes.

The chelating behavior of the components added to the Zn precursor solution were studied by DOSY experiments of non-heated ink. Comparing the diffusion coefficient of the components in a metal-ion free blank and the Zn precursor solution confirmed that Zn acetate and formate complexes are present (Fig. S.1).

In a next step, the films were gradually heated on the hotplate and subsequently examined with ATR-IR where a changing chemical composition could be seen (Fig. 3). As a function of temperature new components are formed. Compared to the FTIR spectra of the sample dried at 90 °C, new vibration modes at 1650 and 1242 cm^{-1} are noticed for samples dried at 120, 150, 200 and 250 °C. The peak at 1650 cm^{-1} can be assigned to the amine bending mode of ethanolamine (1648 cm^{-1}), the vibration mode of surface trapped or adsorbed water (1658 cm^{-1}) or amides but these are not present in the precursor mixture [27,28]. However, the increasing intensity of this peak with increasing temperature (up till 200 °C) suggests that adsorbed water can be excluded. Although, ethanolamine is present in high concentration, the bending mode of this amine was not visible at low temperatures. From 120 °C on, other modes of the amine group (e.g. the mode at 1010 cm^{-1}) are reduced. Next to ethanolamine, the IR active modes of formic acid and zinc acetate such as the ν_a and δ (COO) of formic acid at 1585 cm^{-1} and 762 cm^{-1} and ν_a (COO) of zinc acetate at 1585 cm^{-1} are decreasing as a function of temperature. This can be a result of the thermal removal of the components. Concluding, the vibration modes at 1650 and 1242 cm^{-1} must be assigned to the appearance of new components formed during the heating of the ink.

1D proton NMR was used to identify the new-formed products. To avoid interference of non-contributing chemicals such as malonic acid and aluminium nitrate, only the Zn solution was studied because the formation of new components also took place when the ink did not contain any Al precursor solution. By comparing 1D proton NMR measurements of the solution before and after heating at 120 °C for 1 h (Fig. 4), an insight of the chemical reaction happening during heating could be obtained. Before heating, all components as mixed in the solution are observed in the NMR spectrum, while heating induced signals of 2 additional

Table 1
Overview of the FTIR spectra for the ink: peak assignment according to the specific vibration of the IR active groups.

Vibration mode	Metal-ion free blank (cm^{-1})	Zn prec. sol. (cm^{-1})
ν_a (COO) formic acid and acetic acid	1550	1574
δ (CH_2) ethanolamine	1454w	1454w
ν_s (COO) acetic acid	1406sh	
δ (CH) formic acid	1372	1384
ν_s (COO) formic acid and δ (CH_3) acetic acid	1340	1336
ρ_r (CH_2) ethanolamine	1280sh	1280sh
δ (C-O) ethanolamine	1148	1154
ρ_r (CH_3) acetic acid and ν (C-O) ethanolamine	1070	1068
ρ_r (CH_3) acetic acid and ν (C-N) ethanolamine	1018	1016
ν (C-C) acetic acid	922	930
ν (C-C) ethanolamine	866	866
ρ_r (NH_2) ethanolamine	840	834
δ (COO) formic acid	762	766
δ (COO) acetic acid	652	650
π (CH) acetic acid	616	618

Table 2
Overview of the FTIR spectra of the Al precursor solution: peak assignment according to the specific vibration of the IR active groups.

Vibration mode	Metal-ion free blank (cm^{-1})	Al prec. sol. (cm^{-1})
ν_a (COO) malonic acid	1538	1592
ν_a (COO) formic acid	1538	1538
δ (CH_2) malonic acid	1430sh	1416sh
δ (CH) formic acid	1372sh	1372
ν_s (COO) formic acid and ν (NO_3^-)	1334	1332
ν_s (COO) malonic acid	1334	1308sh
ρ_r (CH_2) malonic acid and ethanolamine	1250	1274
ν_a (C-C) malonic acid and δ (C-O) ethanolamine	1166	/
ν (C-O) ethanolamine	1066	1064
ν (C-N) ethanolamine	1014	1010
ν_s (C-C) malonic acid	976sh	984
ν (Al-OH)	/	964
δ (CH_2) malonic acid	928	948sh
ν (C-C) ethanolamine	868	862

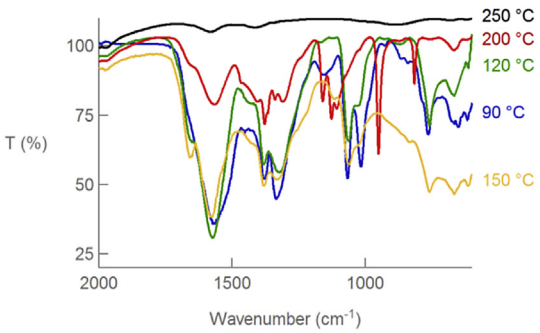

Fig. 3. FTIR spectra of gradually heated thin films on the hotplate at diverse temperatures.

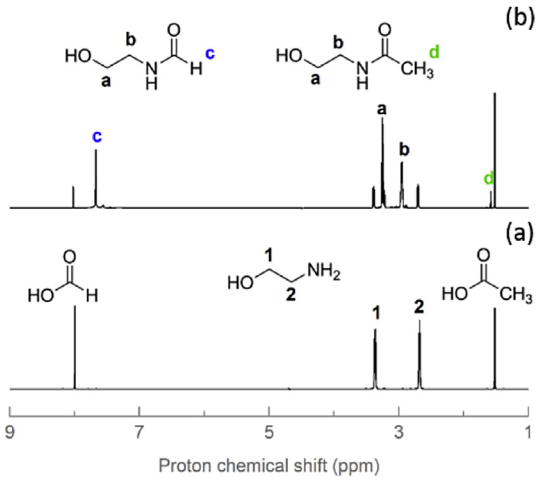

Fig. 4. (a) 1D proton NMR spectrum of Zn precursor solution before heating. (b) 1D proton NMR spectrum of Zn precursor solution after heating at 120 °C for 1 h.

components: N-(2-hydroxyethyl)acetamide and N-(2-hydroxyethyl)formamide. Hence, ethanolamine reacts with acetic acid and formic acid to form their corresponding amides. However, heating of a metal-ion free blank did not result in the formation of amides. Concluding, free acetic acid or formic acid does not react with ethanolamine to their corresponding amide but the Zn chelating acetic acid and formic acid do. In line with the observation of Yang et al. for oleylamine and zinc acetate, the following reaction mechanism is suggested [29]. The amine group of the ethanolamine attacks the electron deficient carbon of the acetate or formate group of the Zn complex resulting in a nucleophilic addition to yield the corresponding amide.

Knowing the identity of the formed component, the peaks appearing in the FTIR spectra at 1650 cm^{-1} and 1242 cm^{-1} can now be assigned to the ν (CO) and δ (NH) of the formed amides.

As illustrated above, drying of the ink induces the formation of amide components, changing the organic composition of the ink (amorphous fraction). A changing amorphous fraction can influence the crystallisation process and affect the final morphology of the thin film [30]. High drying temperatures such as 300 °C can induce the evaporation and elimination of the precursor simultaneously. Medium drying temperatures between 200 °C and 250 °C force the volatile components (water, ethanolamine, non-reacted formic acid) out of the wet film at high rates. At low drying temperatures (<200 °C), the ethanolamine will not evaporate and can react with the formed Zn complexes leading to the formation of the corresponding amides.

The decomposition of the AZO precursor throughout the entire thermal process was monitored by TGA-DTA. 3 major weight losses could be distinguished (Fig. 5). A first mass loss sets in around 150 °C, followed by a mass loss starting around 250 °C and a final mass loss starting at 400 °C. The mass loss observed before 150 °C corresponds with the loss of volatile solvents such as water and non-coordinating components such as formic acid. The step from 150 °C is due to the evaporation of ethanolamine, which has a boiling point of 170 °C, and the formed amides, with a boiling point around 155 °C. The mass loss around 250 °C can be ascribed to the decomposition of the Zn complexes since zinc acetate and zinc formate are known to decompose around 250 °C [31,32]. The mass step after 400 °C can be ascribed to the decomposition of remaining carbon compounds resulting in the final oxides.

The above mentioned results clearly show that the drying

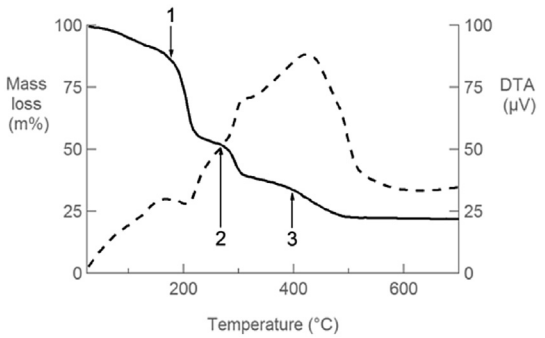

Fig. 5. Thermogravimetric analysis of the ink after drying at 75 °C.

temperature has an effect on the decomposition behaviour and this is reflected in the resistivity of the films. It is known from literature that a good film morphology is of utmost importance to enhance the conductivity of the film. SEM micrographs (Fig. 7) show that the morphology of the AZO thin film is altered from microcracking (dried at 90 °C) to more densified structures (dried at 120–150 °C), to less connected 'isles' of AZO (sample dried at 200–250 °C), or to a grainy structure where the small grains are loosely stacked on each other (dried at 300 °C). Furthermore, the crystallinity (Fig. 6) shows an uniaxial texture along the *c*-axis for the samples dried from 90 till 250 °C. Samples dried at 300 °C exhibit a less textured growth which may be associated with a lower conductivity. It is believed that a more prominent preferential growth along the *c*-axis leads to a reduction of the number of defects and stacking faults at the grain boundaries, which reduces grain boundary scattering and is reflected in the electrical properties. This will result in a higher conductivity of the AZO thin films as the mobility of the charge carriers can be increased. Calculation of the crystallite size (Fig. 6 – inset) shows a variation upon increasing drying temperature. The crystallite size drops to 15 nm at 150 °C and rises again upon increasing temperature. A smaller crystallite size can be caused by defect formation due the more effective Al doping. This is confirmed by the resistivity measurement. The deterioration of the grain size can be attributed to aluminium doping in ZnO films [33].

The differences in morphology also affect the optical properties (Fig. 8) of the final films. Although the transmittance in the visible range is comparable to the bare substrate, the highest transmittance is found for the sample treated at 120 °C.

Looking in detail to the different samples the following trends can be observed. In comparison to the other samples, the sample dried at 300 °C has indeed an inferior resistivity. The morphology of this film exists out of small, loosely stacked grains which enhances grain boundary scattering. The XRD spectrum exhibits reflections of ZnO at 31.79°, 34.36° and 36.20° (JCPDS 89-7102) and most likely of Al_2O_3 at 38.10° (JCPDS 85-1337). The random microcrystal orientation of the AZO film will increase the number of defect and stacking faults at the grain boundaries [17,29,27,32–34]. The reflection of Al_2O_3 even indicates that doping of the ZnO matrix was not successful and a secondary phase is formed. Segregation of this secondary phase at the grain boundaries is expected and will hamper the mobility of the charge carriers [35]. It also indicates that the amount of charge carriers is reduced due to the negligible

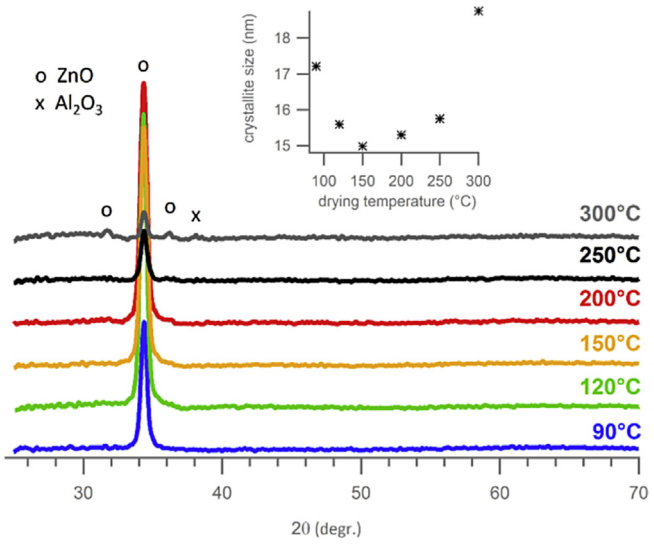

Fig. 6. XRD patterns as a function of the drying temperature.

substitutional doping of Al which is reflected by the larger grain size. This all is a consequence of the high drying temperature. The evaporation of the solvents and additives plus the decomposition of the complexes will occur simultaneously. This may result in many nucleation sites of ZnO and a final morphology with small grains. The high drying temperature also favours the formation of Al_2O_3 instead of the substitution of Al inside the ZnO matrix. The evaporation and decomposition of the precursors at the same time can induce different reaction paths what in this case is introducing Al_2O_3 nuclei.

The morphology of samples dried at 200 °C and 250 °C 2 do not differ a lot. However, drying at 250 °C had a huge effect (x 1000) on the resistivity of the sample. Mainly, this can be attributed to lack of texture of the sample dried at 250 °C. Similar to the sample dried at 300 °C, a small fraction of the dopant may have formed a secondary phase due to the high drying temperature, but here XRD measurements could not confirm the presence of such crystalline phase (Al_2O_3). However, the presence of amorphous alumina can not be excluded.

Samples dried at 90 °C have a resistivity 3 times as high as when dried at 120 °C. The morphology at 90 °C shows microcracks which limit the conduction pathways of the free charge carriers. The drying step may induce these microcracks. Samples dried at 90 °C still have a large part of the non-chelating additives (formic acid and ethanolamine) present inside the thin film as confirmed by the FTIR measurements (Fig. 4). During the thermal treatment in the tube furnace the remaining additives will be removed too fast, resulting in strain and stress which can be released by crack formation. However, drying at higher temperatures (120 °C–150 °C) prevented this as no microcracks can be seen in the other samples. At these temperatures ethanolamine, indeed, has already been partially removed and crack formation will be avoided.

The sample dried at 150 °C has comparable electrical properties as when dried at 120 °C. Similar morphologies and crystallinity were obtained. Nevertheless, drying at 120 °C results in areas which are more densified giving rise to slightly better electrical properties.

Summarising, the drying temperature clearly influences the decomposition products, morphology, crystallinity and electrical properties of these AZO thin films. High drying temperatures (300 °C) resulted in a flash evaporation of the unreacted components together with the decomposition of the formed complexes. This led to the formation of unwanted secondary phases (Al_2O_3), while drying at lower temperatures (200–250 °C) only resulted in the flash evaporation of the unreacted components. Drying at 90 °C led to the formation of microcracks and an optimum was found when the samples were dried at 120 °C.

3.2. Dry vs wet processing of AZO thin films

As concluded in the previous paragraphs, improved properties were obtained after drying the wet films on a hotplate at 120 °C. However, the electrical properties of the TCO material need further improvement. Some respected literature states that a wet atmosphere could be beneficial during thermal processing [22,36,37]. As can be seen in Table 3, the varying water vapour partial pressure, which is controlled by the water temperature, has an effect on the electrical properties. A minimal resistivity is obtained with a water vapour enriched atmosphere at 20 °C.

As mentioned before, the electrical properties are closely related to morphology and crystallinity of these films. The morphology of the AZO thin films depends on the partial vapor pressure of water as shown in Fig. 9. It is noticed that the top morphology changed by varying water vapour enriched atmospheres. Generally, larger grains are observed by wet processing. This is in line with the

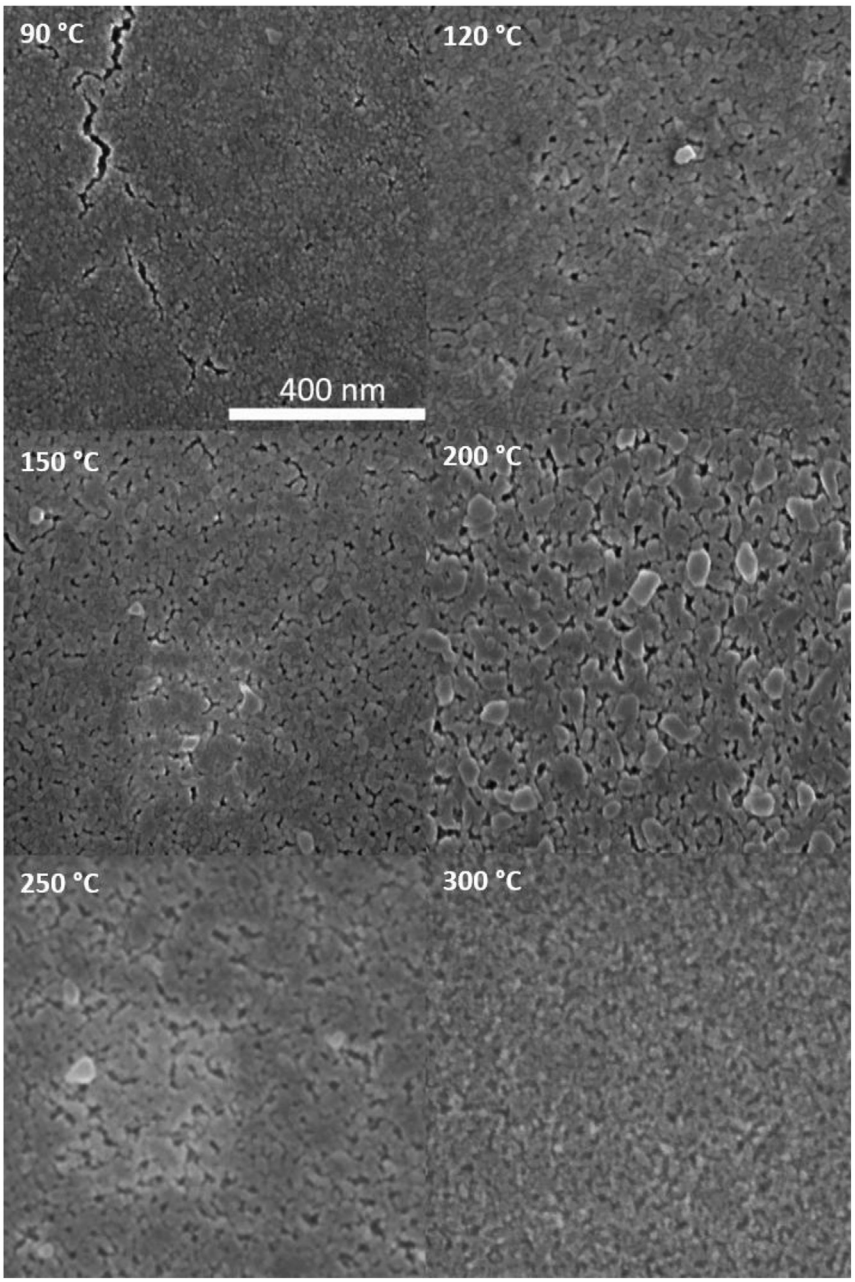

Fig. 7. SEM images of AZO thin films dried on different temperatures.

observation of Nakada et al. where grain growth is induced by water vapour [38]. Compared to an annealed layer in dry atmosphere a more porous/less connected morphology was observed for samples treated with an atmosphere bubbled through water at 10 and 30 °C. The sample exposed to a humid atmosphere created with water at 20 °C resulted in a more dense structure.

Also, the film texture is affected by varying processing conditions (Fig. 10). Indeed, the intensity of the (002)-reflection is increased by adding water vapour during processing. However, sample (30 °C) exhibits more random microcrystal orientation as the (100), (002) and (101)-reflections (31.79°, 34,45° and 36.20° (JCPDS 89-7102)) can be distinguished in the XRD patterns. These (100) and (101)-reflections can also be seen for sample (20 °C) but at much lower intensities. Altogether, samples prepared with 200 ppm O_2/N_2 bubbled through water at 20 °C show the best electrical properties, coupled with a rather dense top morphology and a high intensity of the (002)-reflection, even though low intensity diffractions peaks located at the 31.79° and 36.20° are also present.

To have a better understanding of the influence of a wet atmosphere during thermal processing on the incorporation of Al in the ZnO matrix, synthesised AZO bulk powders were analysed by 1 D ^{27}Al MAS NMR (Fig. 11). Generally, hexacoordinated octahedral Al is observed at 0 ± 15 ppm (VI), while 4-fold coordinated tetrahedral Al is observed at 65 ± 15 ppm (IVa and IVb) and pentacoordinated Al is observed at 30 ± 15 ppm (V) [10,39]. As mentioned in the introduction, Al can occupy 2 types of tetrahedral sites: Al^{3+} ions can substitute Zn^{2+} ions in the ZnO matrix, occupying a tetrahedral site in the crystal lattice (IVa), while Al^{3+} ions can also occupy empty tetrahedral sites (IVb). Substitutional Al is positioned in a

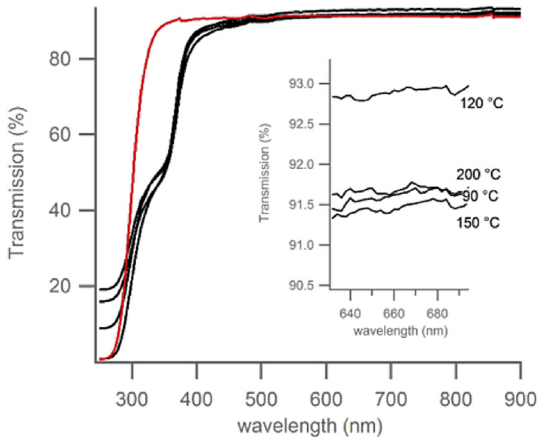

Fig. 8. UV–Vis measurements of AZO samples dried at 90 °C – 200 °C. The red line indicates the bare substrate. The inset shows a magnication of the region 620–700 nm. (For interpretation of the references to colour in this figure legend, the reader is referred to the web version of this article.)

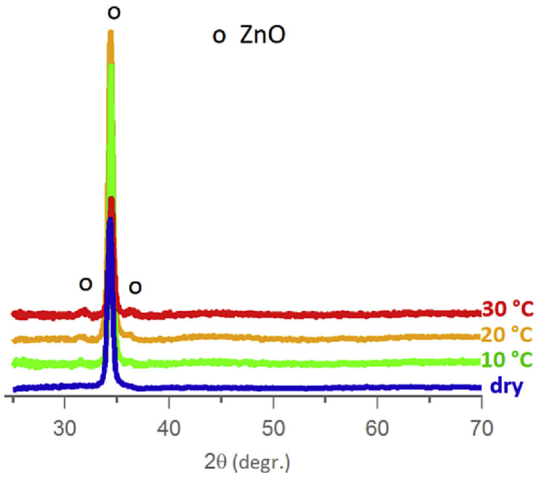

Fig. 10. XRD patterns of AZO thin films undergoing a thermal oxidation with a gas atmosphere bubbled through water at different temperatures.

Table 3
The resistivity as a function of the gas atmosphere bubbled through water at different temperatures.

Water temperature °C	Resistivity Ω cm
dry	1.91×10^{-1}
10	9.61×10^{-2}
20	2.54×10^{-2}
30	2.64×10^{-1}

highly symmetrical tetrahedral site resulting in a narrow line without any quadrupolar line shape, while a broad signal correlates with the distorted or amorphous environment of an empty tetrahedral site [10,40,41]. Dry processed AZO powders were compared with powders synthesised according to the most optimised conditions as discussed above. As illustrated in Fig. 11, both spectra show a sharp signal at 81 ppm, much broader signals centred at 69 ppm and 42 ppm and a broad signal with its centre at 10 ppm.

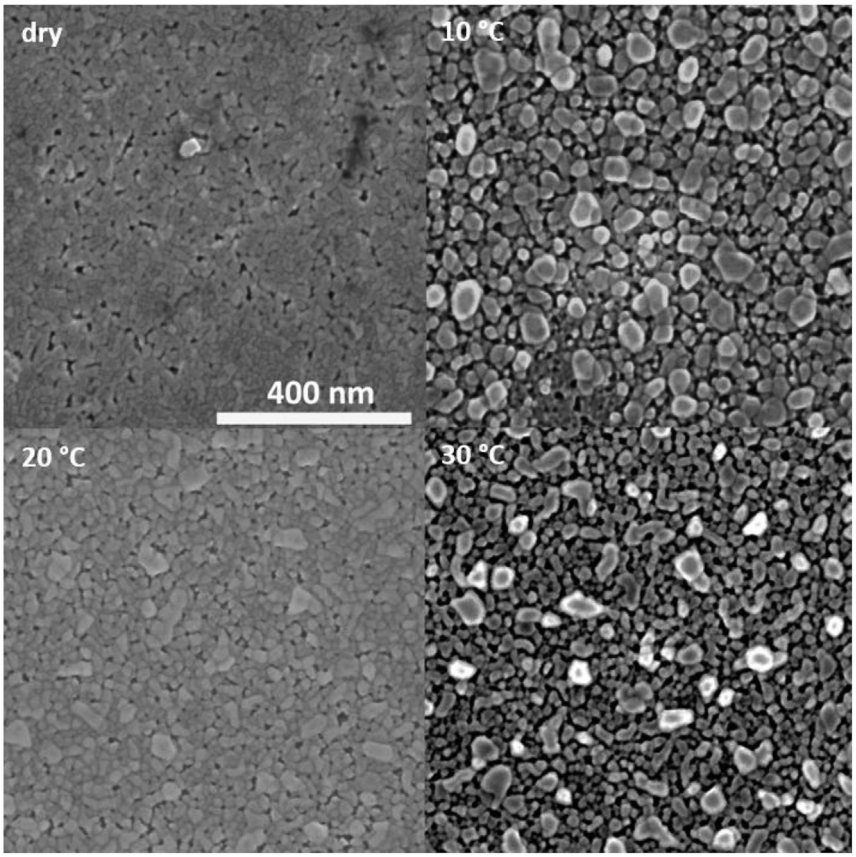

Fig. 9. SEM images of AZO thin films oxidative treated with the gas atmosphere bubbled through water at different temperatures.

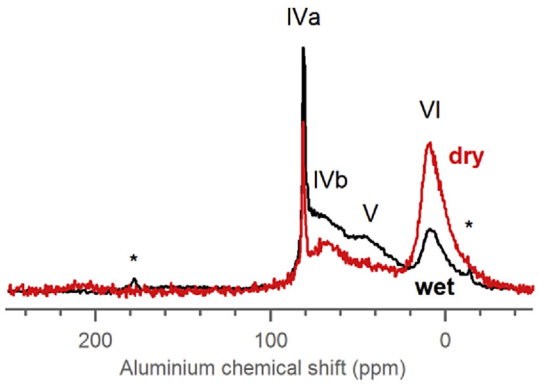

Fig. 11. 1D^{27}Al MAS NMR spectra of bulk powders samples obtained by heating AZO ink in a) dry air and b) wet air at 500 °C for 1 h, where * marks spinning sidebands.

can induce another reaction route or faster decomposition of the precursor leading to a thin film with improved properties. Introduction of too much water vapour in the processing atmosphere can enhance these reactions and/or the kinetics of the oxidation even more. This may lead to an uncontrolled reaction route resulting in AZO coatings with poorer properties, e.g. sample prepared with the gas atmosphere bubbled through water at 30 °C.

4. Conclusion

The electrical properties of AZO thin films deposited by a single print step of an aqueous ink can be optimised by varying the processing conditions. (1) The influence of the drying temperature was studied. An optimal drying temperature of 120 °C was obtained, resulting in a denser top morphology and high *c*-axis preferential growth. Other drying temperatures resulted in a more porous structure or led to the formation of microcracks. This variation in the structural and electrical properties can be explained by a change in composition of the amorphous fraction during the drying procedure. (2) The thermal process is further changing the humidity of the processing atmosphere. Generally, wet processing resulted in AZO thin films with larger grains. Bubbling the atmosphere through 2 glass bottles containing water at 20 °C led to AZO thin films with an resistivity of 2.54×10^{-2} Ω cm. These thin films showed a higher preferential growth of the *c*-axis and a denser morphology. Compared to dry processed AZO bulk powders, wet processed AZO bulk powder contains less octahedral coordinated Al and more substitutional Al, resulting in more charge carriers and less electron acceptor states. Concluding, wet processing not only affects the morphology and crystallinity but also the incorporation of the Al inside the ZnO matrix.

Table 4
Representation of the relative Al distribution in the ZnO matrix obtained by the deconvolution of the 1D^{27}Al MAS NMR spectra.

	6-Fold coordinated	5-Fold coordinated	4-Fold coordinated	
	VI	V	Substitutional IVa	Interstitial IVb
Dry	53.3%	20.5%	6.6%	19.6%
Wet	22.4%	38.6%	9%	30%

The narrow distribution at 81 ppm can be assigned to substitutional Al (IVa), while the broad distribution at 69 ppm is assigned to Al occupying 'empty' tetrahedral sites (IVb). 6-fold octahedrally coordinated Al is assigned to the signal centred at 10 ppm (VI). The signal centred at 42 ppm could be assigned to 5-fold coordinated Al or distorted tetrahedral coordination. Most likely, a combination of both situations occurs, penta-coordinated and distorted tetra-coordinated Al [40]. The signals in the 1D^{27}Al MAS NMR spectra were deconvoluted by constructing Gaussian/Lorentzian envelopes at the different peaks. Table 4 shows the relative distribution of the Al in the ZnO matrix.

Wet processed AZO has less hexacoordinated octahedral and more substitutional Al present in the ZnO matrix than dry processed AZO (Table 4). This can result in more charge carriers as substitutional Al can donate electrons to the conduction band of ZnO. Fewer octahedral sites occupied by Al benefit for the conductivity, as fewer electron acceptor sites can trap free charge carriers. Overall, a positive contribution to the carrier density is observed. Combined with higher preferential growth of the *c*-axis and relative denser morphology, the mobility of these charge carriers is increased as well (Table 5).

These results show that wet processing of AZO thin films did not only influence the morphology and crystallinity, but the incorporation of Al in the ZnO matrix as well. This indicates that the humidity of the processing atmosphere promotes substitutional incorporation in the ZnO structure. A change in humidity can, indeed, influence the decomposition and the reaction between the formed reactive oxide species during the thermal process [42]. Also, the absorption and easier breakup of water vapour at the surface of the thin film can accelerate the kinetics of the oxidation [43]. This

Table 5
Overview of the electrical properties of dry and wet processed thin films as determined by Hall-Van der Pauw measurements.

	Resistivity Ω cm	Mobility cm^2 V^{-1} s^{-1}	Carrier density cm^{-3}
Dry	1.91×10^{-1}	5	6.51×10^{18}
Wet	2.54×10^{-2}	11	2.23×10^{19}

Acknowledgment

The authors would like to thank Olivier Janssens for performing the XRD measurements. K.D.B and K.V. thank UGent (Research grant 01N01412). J. D. R. thanks the FWO for his predoctoral fellowship. C.E.A.K. acknowledges the Flemish government for long-term structural funding (Methusalem).

Appendix A. Supplementary data

Supplementary data related to this article can be found at http://dx.doi.org/10.1016/j.jallcom.2016.08.120.

References

[1] C. Thiele, R. Das, Transparent Conductive Films (TCF) 2012-2022: Forecasts, Technologies, Players, 2013, p. 159.
[2] C.A. Hoel, T.O. Mason, J.-F. Gaillard, K.R. Poeppelmeier, Transparent conducting oxides in the ZnO-In_2O_3-SnO_2 system, Chem. Mat. 22 (2010) 3569–3579.
[3] Y.L. Liu, Y.F. Li, H.B. Zeng, ZnO-based transparent conductive thin films: doping, performance, and processing, J. Nanomater (2013) 9.
[4] T. Minami, H. Sato, H. Nanto, S. Takata, Group-III impurity doped zinc-oxide thin-films prepared by RF magnetron sputtering, Jpn. J. Appl. Phys. Part 2-Lett. 24 (1985) L781–L784.
[5] G.J. Exarhos, X.-D. Zhou, Discovery-based design of transparent conducting

oxide films, Thin Solid Films 515 (2007) 7025–7052.
[6] M. Bazzani, A. Neroni, A. Calzolari, A. Catellani, Optoelectronic properties of Al: ZnO: Critical dosage for an optimal transparent conductive oxide, Appl. Phys. Lett. 98 (2011) 3.
[7] T. Minami, T. Yamamoto, T. Miyata, Highly transparent and conductive rare earth-doped ZnO thin films prepared by magnetron sputtering, Thin Solid Films 366 (2000) 63–68.
[8] H.-l. Shen, H. Zhang, L.-f. Lu, F. Jiang, C. Yang, Preparation and properties of AZO thin films on different substrates, Prog. Nat. Sci. Mater. Int. 20 (2010) 44–48.
[9] F. Maldonado, A. Stashans, Al-doped ZnO: electronic, electrical and structural properties, J. Phys. Chem. Solids 71 (2010) 784–787.
[10] T. Kemmitt, B. Ingham, R. Linklater, Optimization of sol-gel-formed ZnO: Al processing parameters by observation of Dopant Ion location using solid-state Al-27 NMR spectrometry, J. Phys. Chem. C 115 (2011) 15031–15039.
[11] H. Serier, M. Gaudon, M. Menetrier, Al-doped ZnO powdered materials: Al solubility limit and IR absorption properties, Solid State Sci. 11 (2009) 1192–1197.
[12] H. Agura, A. Suzuki, T. Matsushita, T. Aoki, M. Okuda, Low resistivity transparent conducting Al-doped ZnO films prepared by pulsed laser deposition, Thin Solid Films 445 (2003) 263–267.
[13] S.-M. Park, T. Ikegami, K. Ebihara, Effects of substrate temperature on the properties of Ga-doped ZnO by pulsed laser deposition, Thin Solid Films 513 (2006) 90–94.
[14] R.M. Pasquarelli, D.S. Ginley, R. O'Hayre, Solution processing of transparent conductors: from flask to film, Chem. Soc. Rev. 40 (2011) 5406–5441.
[15] H. Damm, P. Adriaensens, C. De Dobbelaere, B. Capon, K. Elen, J. Drijkoningen, B. Conings, J.V. Manca, J. D'Haen, C. Detavernier, P. Magusin, J. Hadermann, A. Hardy, M.K. Van Bael, Factors influencing the conductivity of aqueous sol(ution)-gel-processed Al-Doped ZnO films, Chem. Mat. 26 (2014) 5839–5851.
[16] W. Tang, D.C. Cameron, Aluminium-doped zinc-oxide transparent conductors deposited by the sol-gel process, Thin Solid Films 238 (1994) 83–87.
[17] M. Ohyama, H. Kozuka, T. Yoko, Sol-gel preparation of ZnO films with extremely preferred orientation along (002) plane from zinc acetate solution, Thin Solid Films 306 (1997) 78–85.
[18] Y. Natsume, H. Sakata, Zinc oxide films prepared by sol-gel spin-coating, Thin Solid Films 372 (2000) 30–36.
[19] J. Feys, P. Vermeir, P. Lommens, S.C. Hopkins, X. Granados, B.A. Glowacki, M. Baecker, E. Reich, S. Ricard, B. Holzapfel, P. Van der Voort, I. Van Driessche, Ink-jet printing of $YBa_2Cu_3O_7$ superconducting coatings and patterns from aqueous solutions, J. Mat. Chem. 22 (2012) 3717–3726.
[20] B. Derby, Inkjet printing of functional and structural materials: fluid property requirements, feature stability, and resolution, in: D.R. Clarke, M. Ruhle, F. Zok (Eds.), Ann. Rev. Mat. Res, 2010, pp. 395–414.
[21] C.J. Brinker, G.W. Scherer, Sol-gel Science: the Physics and Chemistry of Sol-gel Processing, Academic Press, Boston, 1990.
[22] G. Pollefeyt, S. Clerick, P. Vermeir, P. Lommens, K. De Buysser, I. Van Driessche, Influence of aqueous precursor chemistry on the growth process of epitaxial SrTiO3 buffer layers, Inorg. Chem. 53 (2014) 4913–4921.
[23] T.T. Thuy, S. Hoste, G.G. Herman, K. De Buysser, P. Lommens, J. Feys, D. Vandeput, I. Van Driessche, Sol-gel chemistry of an aqueous precursor solution for YBCO thin films, J. Sol-Gel Sci. Technol. 52 (2009) 124–133.
[24] K. Vernieuwe, J. Feys, D. Cuypers, K. De Buysser, Ink-jet printing of aqueous inks for single-layer deposition of Al-doped ZnO thin fims, J. Am. Ceram. Soc. 1 (2016), http://dx.doi.org/10.1111/jace.14059.
[25] J.F. Chang, W.C. Lin, M.H. Hon, Effects of post-annealing on the structure and properties of Al-doped zinc oxide films, Appl. Surf. Sci. 183 (2001) 18–25.
[26] B.Y. Oh, M.C. Jeong, D.S. Kim, W. Lee, J.M. Myoung, Post-annealing of Al-doped ZnO films in hydrogen atmosphere, J. Cryst. Growth 281 (2005) 475–480.
[27] K.J. Han, K.S. Kang, Y. Chen, K.H. Yoo, J. Kim, Effect of annealing temperature on the conduction mechanism for a sol-gel driven ZnO Schottky diode, J. Phys. D-Applied Phys. 42 (2009).
[28] C. Mondal, M. Ganguly, A.K. Sinha, J. Pal, T. Pal, Fabrication of a ZnO nanocolumnar thin film on a glass slide and its reversible switching from a superhydrophobic to a superhydrophilic state, RSC Adv. 3 (2013) 5937–5944.
[29] H.-J. Yang, S.-Y. He, H.-Y. Tuan, Simultaneous axial screw dislocation-mediated growth and radial layer-by-layer deposition for controlled synthesis of asymmetric axial ZnO nanospindles, Nanoscale 6 (2014) 9034–9042.
[30] S. Fujihara, C. Sasaki, T. Kimura, Crystallization behavior and origin of c-axis orientation in sol-gel-derived ZnO : Li thin films on glass substrates, Appl. Surf. Sci. 180 (2001) 341–350.
[31] A.V. Ghule, K. Ghule, C.-Y. Chen, W.-Y. Chen, S.-H. Tzing, H. Chang, Y.-C. Ling, In situ thermo-TOF-SIMS study of thermal decomposition of zinc acetate dihydrate, J. Mass Spectrom. 39 (2004) 1202–1208.
[32] K. Gyoryova, V. Balek, V. Zelenak, Thermal-stability of zinc formate complex-compounds containing urea, thiourea and caffeine, Thermochim. Acta 234 (1994) 221–232.
[33] J.H. Wang, L. Meng, Y. Qi, M.L. Li, G.M. Shi, M.L. Liu, The Al-doping contents dependence of the crystal growth and energy band structure in Al:ZnO thin films, J. Cryst. Growth 311 (2009) 2305–2308.
[34] K. Maejima, H. Shibata, H. Tampo, K. Matsubara, S. Niki, Correlation between electrical properties and crystal c-Axis orientation of zinc oxide transparent conducting films, Jpn. J. Appl. Phys. 51 (2012).
[35] M. Chen, Z.L. Pei, X. Wang, Y.H. Yu, X.H. Liu, C. Sun, L.S. Wen, Intrinsic limit of electrical properties of transparent conductive oxide films, J. Phys. D. - Appl. Phys. 33 (2000) 2538–2548.
[36] K. Nomura, T. Kamiya, H. Ohta, M. Hirano, H. Hosono, Defect passivation and homogenization of amorphous oxide thin-film transistor by wet O(2) annealing, Appl. Phys. Lett. 93 (2008).
[37] S. Sathyamurthy, K. Kim, T. Aytug, M. Paranthaman, Effect of relative humidity on the crystallization of sol-gel lanthanum zirconium oxide films, Chem. Mat. 18 (2006) 5829–5831.
[38] T. Nakada, Y. Ohkubo, A. Kunioka, Eeffect of water-vapor on the growth of textured ZnO-based films for solar-cells by DC-magnetron sputtering, Jpn. J. Appl. Phys. Part 1-Regular Pap. Short Notes Rev. Pap. 30 (1991) 3344–3348.
[39] K.J.D. MacKenzie, E. Smith, Multinuclear Solid-state Nuclear Magnetic Resonance of Inorganic Materials, Pergamon, Oxford, 2002.
[40] Y.S. Avadhut, J. Weber, E. Hammarberg, C. Feldmann, J.S.a.d Guenne, Structural investigation of aluminium doped ZnO nanoparticles by solid-state NMR spectroscopy, Phys. Chem. Chem. Phys. 14 (2012) 11610–11625.
[41] R. Noriega, J. Rivnay, L. Goris, D. Kaelblein, H. Klauk, K. Kern, L.M. Thompson, A.C. Palke, J.F. Stebbins, J.R. Jokisaari, G. Kusinski, A. Salleo, Probing the electrical properties of highly-doped Al:ZnO nanowire ensembles, J. Appl. Phys. 107 (2010).
[42] E.L. Crepaldi, G. Soler-Illia, D. Grosso, F. Cagnol, F. Ribot, C. Sanchez, Controlled formation of highly organized mesoporous titania thin films: from mesostructured hybrids to mesoporous nanoanatase TiO2, J. Am. Chem. Soc. 125 (2003) 9770–9786.
[43] R. Chen, C. Zou, X. Yan, A. Alyamani, W. Gao, Growth mechanism of ZnO nanostructures in wet-oxidation process, Thin Solid Films 519 (2011) 1837–1844.